International Tables for Crystallography (2018). Vol. H, Chapter 2.2, pp. 51–65.

2.2. Synchrotron radiation and powder diffraction

A. Fitch

2.2.1. Introduction

X-rays produced at a synchrotron source are exploited in a wide range of applications in crystallography and structural science, and this includes studies by powder diffraction. Many synchrotron-radiation facilities have one or more dedicated powder-diffraction beamlines or end stations in regular user service. The high intensity, collimation and wavelength tunability of the radiation allow instruments to be designed whose performance and flexibility surpass what is possible with conventional laboratory apparatus. The majority of instruments operate with monochromatic radiation and an angle-dispersive diffractometer, but the polychromatic nature of synchrotron radiation means that an energy-dispersive setup is also possible. The general properties of synchrotron radiation include:

(*a*) High brightness, *i.e.* a highly collimated, intense X-ray beam and small source size.
(*b*) High flux of photons delivered to the sample.
(*c*) A range of wavelengths is available, possibly extending from the soft to the hard X-ray regimes, depending on the facility.
(*d*) Polarized source: synchrotron radiation is linearly polarized with the electric vector lying in the plane of the synchrotron orbit, but becomes progressively less polarized out of the plane.
(*e*) Pulsed source: the distribution of the bunches of electrons circulating in the storage ring allows the time structure to be exploited for specialized experiments.

Further information about the nature of synchrotron radiation can be found in texts by, for example, Margaritondo (1988), Als-Nielsen & McMorrow (2001) and Kim (2001).

Synchrotrons are usually user facilities, where scientists from external laboratories visit to perform experiments that have been approved by a peer-review or other procedure, and are supported by the scientific and technical staff for the beamlines. Most facilities have regular rounds in which users submit proposals for beam time, with special arrangements for access to carry out proprietary research. Arrangements can also usually be made for urgent access to the facility (when justified), and some beamlines run a routine mail-in service, allowing samples to be measured under defined conditions without the user needing to attend.

For any powder X-ray diffraction experiment, the wavelength of the radiation to be used is of high importance. The wavelength, λ, is a measure of the photon energy, ε, and the terms 'photon energy' and 'wavelength' tend to be used interchangeably at synchrotron beamlines. They can readily be converted by

$$\varepsilon = h\nu = hc/\lambda,$$

where h is the Planck constant, ν is the frequency of the radiation and c is the speed of light. If expressed in convenient units with λ in Å and ε in keV then

$$\varepsilon\ [\text{keV}] = hc/e\lambda \times 10^7\ [\text{Å}] \simeq 12.3984/\lambda\ [\text{Å}] \simeq 12.4/\lambda\ [\text{Å}],$$

where e is the elementary charge.

2.2.2. Production of synchrotron radiation

Synchrotron radiation is emitted by charged particles travelling at relativistic speeds when they are accelerated to move in a curved trajectory. In a modern synchrotron facility dedicated to the production of X-ray beams for scientific experiments, electrons are circulated in a closed horizontal orbit in a storage ring at an energy of several GeV, steered by magnetic fields from bending magnets. The overall circumference of the orbit can be several hundred metres depending on the design and specifications of an individual ring. The synchrotron ring is built up of cells (Fig. 2.2.1) comprising a straight section and a bending magnet by which the electrons are guided into the following straight section. Beamlines emerge tangentially from the bending magnets where synchrotron radiation is emitted by the electrons as they curve from one straight section into the next. Beamlines are also constructed on the straight sections where insertion devices, arrays of magnets providing an alternating magnetic field, are placed to cause the path of the electrons to oscillate and so also emit synchrotron radiation. By choosing the period of the magnetic array and by varying the strength of the magnetic field, the wavelength distribution and divergence of the X-rays emitted from an insertion device can be controlled. A straight section may accommodate more than one insertion device in series, allowing greater intensity or flexibility in the emitted radiation for the associated beamline. In the storage ring, the energy that the electrons lose by emitting synchrotron radiation is replaced by coupling the electrons to radio-frequency radiation supplied from klystrons or solid-state devices. Thus the synchrotron facility converts electrical energy, *via* radio waves and relativistic electrons, into powerful beams of electromagnetic radiation.

One key parameter of a storage ring is the energy of the circulating electrons. The energy of an electron moving with

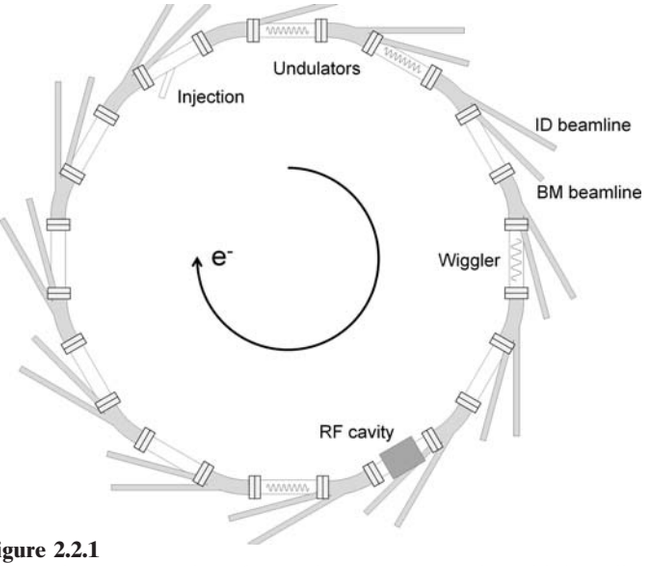

Figure 2.2.1
Schematic representation of a synchrotron storage ring with beamlines radiating tangentially from the bending magnets and in line with the straight sections. ID = insertion device, BM = bending magnet; RF = radio-frequency.

speed v is

$$E_e = \frac{m_e c^2}{(1 - v^2/c^2)^{1/2}} = \gamma m_e c^2,$$

where m_e is the rest mass of the electron, $9.10938356\,(11) \times 10^{-31}$ kg. The term $1/(1 - v^2/c^2)^{1/2}$ is referred to as γ and is the factor by which the mass of the electron increases from its rest mass because of its relativistic speed. Expressed in eV (the conversion factor from kg to eV is c^2/e), the electron rest mass is $5.109989461\,(31) \times 10^5$ eV, so that

$$\gamma \simeq 1957 E_e \text{ [GeV]}$$

when E_e is given in the customary units of GeV. Thus for a 3-GeV machine, a common energy for a synchrotron-radiation source, γ has the value of 5871. The mass of an electron with energy 3 GeV is therefore 3.22 atomic mass units, so around 7% more massive than a stationary atom of ^{3}H or ^{3}He.

Electrons do not circulate individually in the storage ring but in a series of bunches that are in phase with the accelerating radio frequency. Radiation is therefore emitted in pulses as each bunch passes through a bending magnet or insertion device. Thus the number and distribution of the electron bunches around the orbit determine the time structure of the emitted radiation. For most powder-diffraction applications using synchrotron radiation, the pulsed nature of the source can be neglected and the radiation can be regarded as continuous, although attention should also be paid to the performance of detectors that are more susceptible to pulse pile-up problems when the radiation arrives at very high average rates or in concentrated bursts (Cousins, 1994; Laundy & Collins, 2003; Honkimäki & Suortti, 2007), which can happen with certain bunch-filling modes. Certain specialized experiments requiring very fast time resolution can exploit the time structure of the source. In such experiments the longitudinal dimension of the bunches controls the pulse duration, which is usually a few tens of picoseconds.

In discussing the performance of different beamlines, the spectral brightness (Mills *et al.*, 2005) is often quoted for the source and is defined as

spectral brightness =

photons per second per 0.1% bandwidth per mrad^2 per mm^2,

where '0.1% bandwidth' represents $\delta\lambda/\lambda = 0.001$, the mrad^2 term expresses the solid-angle of the emission of the X-rays from the source and the mm^2 term relates to the cross-sectional area of the source. Thus a source of high spectral brightness emits many photons per second of the specified energy, into a narrow solid angle, with a small source size. The source size, which may well differ in the horizontal and vertical directions, is an important consideration as source size and beam divergence ultimately limit the performance of the beamline optical system in terms of collimation, energy resolution and focal spot size.

2.2.2.1. *Bending magnets*

A bending magnet provides a vertical magnetic field to deflect the electrons laterally in the horizontal plane from a straight-line trajectory, and thereby causes the emission of synchrotron radiation (see Fig. 2.2.2). The lateral Lorentz force, F, acting on an electron travelling at velocity v in a magnetic field B is mutually perpendicular to both the magnetic field and the direction of travel of the electron, and is given by

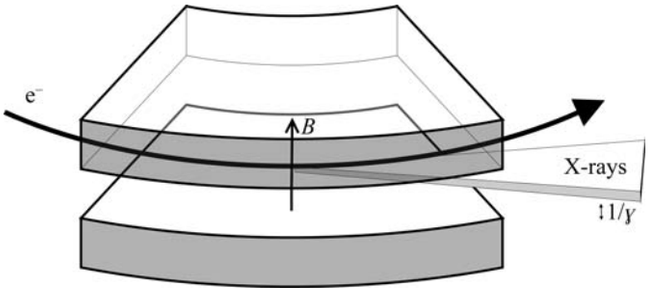

Figure 2.2.2
Emission of a fan of radiation by the electron beam as it curves in a bending magnet from one straight section of the ring to the next.

$$F = evB.$$

In a bending magnet the magnetic field is applied over an extended distance leading to a curved path of radius ρ. The centripetal acceleration is $F/\gamma m_e$, which for circular motion is equal to v^2/ρ. Since $v \simeq c$,

$$\rho = \frac{\gamma m_e c}{eB},$$

so the radius of curvature decreases with magnetic field strength and increases with machine energy *via* increased γ. With the electron energy expressed in GeV, this can be approximated to $\rho \simeq 3.34 E_e$ [GeV]$/B$ (where $10^9/c \simeq 3.34$).

Synchrotron radiation is emitted in a forward cone tangential to the direction of the electrons' motion (Fig. 2.2.3) with a nominal Gaussian distribution and an opening angle of the order of $1/\gamma$. Thus the radiation is highly collimated in the vertical plane. In the horizontal plane, synchrotron radiation is emitted in a broad fan, tangential to the curved trajectory of the electrons as they sweep through the bending magnet. Only a fraction of the radiation emitted by a bending magnet enters the associated beamline *via* a cooled aperture defining a horizontal acceptance angle of a few mrad. The radiation is polarized in the plane of the synchrotron orbit. Sometimes, more than one beamline can be built on a bending magnet with a suitable angular separation between them.

Photons are emitted over a broad spectral range. The critical photon energy, ε_c, divides the emitted power into equal halves and is given by

$$\varepsilon_c = \frac{3\hbar c\gamma^3}{2\rho} = \frac{3\hbar\gamma^2 eB}{2m_e} = \frac{3\hbar e E_e^2 B}{2m_e^3 c^4} = 4.151 E_e^2 B,$$

or, with photon and electron energies in keV and GeV, respectively,

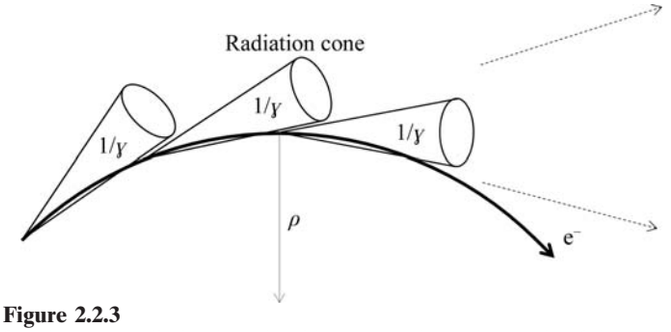

Figure 2.2.3
Synchrotron radiation is emitted in a cone of opening angle of the order of $1/\gamma$ tangential to the electrons as they follow a curved trajectory through the bending magnet.

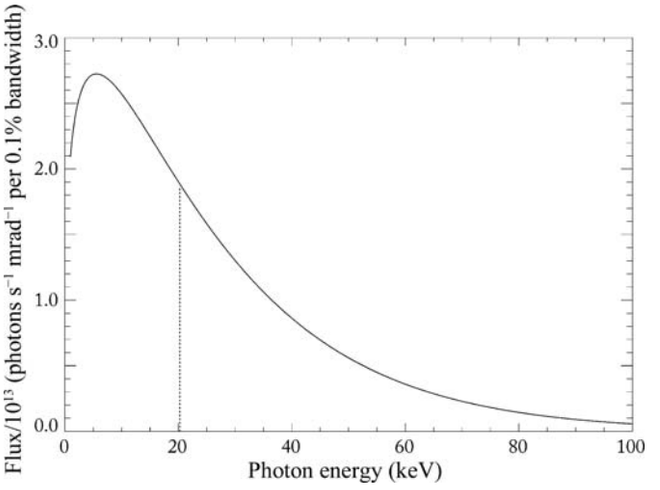

Figure 2.2.4
Spectrum of a bending magnet (B = 0.85 T) at the ESRF with an electron energy of 6 GeV (γ = 11 742), shown as flux per horizontal mrad for a 0.1% energy bandwidth at a storage-ring current of 200 mA. The critical energy of 20.3 keV divides the emitted power into equal halves.

$$\varepsilon\ [\mathrm{keV}] = 0.665 E_e^2\ [\mathrm{GeV}] B.$$

The higher the critical energy, the greater the number of photons produced with short X-ray wavelengths. As an example, consider a bending magnet at the ESRF in Grenoble, France, which has a 6-GeV storage ring and bending magnets with a field of 0.85 T. The bending radius is 23.5 m and the critical photon energy is 20.3 keV (equivalent to a wavelength of 0.61 Å). The spectrum of such a device is shown in Fig. 2.2.4.

The vertical collimation of the radiation varies with photon energy in a nonlinear manner (Kim, 2001). Nevertheless, the divergence decreases with increased photon energy, so beams with the shortest wavelengths are the most vertically collimated. Various approximations can be written to describe the variation, such as for a single electron (Margaritondo, 1988),

$$\sigma_v(\varepsilon) \simeq \frac{0.565}{\gamma}\left(\frac{\varepsilon_c}{\varepsilon}\right)^{0.425},$$

where $\sigma_v(\varepsilon)$ is the standard deviation of the vertical-divergence distribution of photons of energy ε. For a population of electrons circulating in a storage ring, the distribution of the trajectories with respect to the plane of the orbit (of the order μrad) must also be considered, as these add to the vertical emission distribution. An approximation such as

$$\Psi_v(\varepsilon) = 2\sigma_v(\varepsilon) \simeq \frac{1.2}{\gamma}\left(\frac{\varepsilon_c}{\varepsilon}\right)^{1/2}$$

will often be adequate to estimate the vertical divergence Ψ_v in the vicinity of ε_c. Thus for the bending magnet illustrated in Fig. 2.2.4, photons at the critical energy of 20.3 keV will have a vertical divergence of ∼100 μrad. A beamline would probably accept less than this, *e.g.* a 1.5-mm-high slit at 25 m from the source defining the beam onto a monochromator crystal defines an angle of ∼60 μrad.

2.2.2.2. *Insertion devices*

Insertion devices can be classified into two main types, termed 'wigglers' and 'undulators', illustrated in Fig. 2.2.5. A wiggler has a relatively long magnetic period and the radiation from each oscillation is emitted like a series of powerful bending magnets, summing together to provide increased intensity. An undulator has a relatively short magnetic period and the radiation from sequential oscillations interferes coherently to give modified beam characteristics.

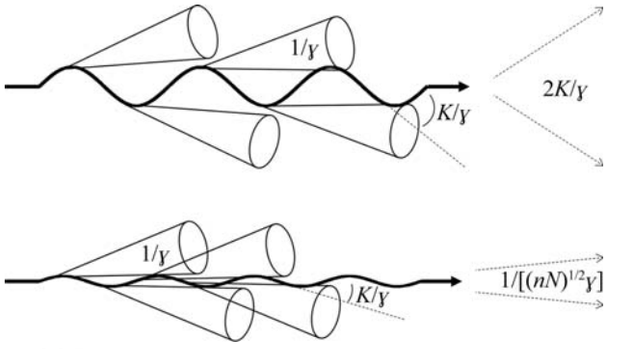

Figure 2.2.5
Schematic illustration of a wiggler (upper) and an undulator (lower).

For insertion devices the magnetic field acting on the electrons varies sinusoidally along the device,

$$B(z) = B_0 \sin(2\pi z/\lambda_u),$$

where B_0 is the peak magnetic field, z is the distance along the insertion-device axis and λ_u is the magnetic period. With a vertical field, the alternating magnetic field causes the electron path to oscillate in the horizontal plane. Note that the radiation is emitted mainly towards the outsides of the oscillations where the electrons change transverse direction, and where the magnetic field and beam-path curvature are highest. The maximum angular deflection of an electron from the axis of the insertion device is K/γ, where the deflection parameter K is given by

$$K = \frac{eB_0\lambda_u}{2\pi m_e c},$$

which simplifies to $K = 0.0934 B_0 \lambda_u$ [mm] with λ_u expressed in mm. K is a crucial parameter that determines the behaviour of the insertion device.

2.2.2.2.1. *Wigglers*

If K is large (10 or above), the insertion device is a wiggler and the electrons oscillate with an amplitude significantly greater than the emitted radiation's natural opening angle $1/\gamma$. Every oscillation along the device produces a burst of synchrotron radiation and these add together incoherently so increasing the flux in proportion to the number of magnetic periods. The radiation emerges from the wiggler in a horizontal fan with a horizontal opening angle $\sim 2K/\gamma$. The intensity of a wiggler-based beamline can be very high because each oscillation produces synchrotron radiation, and this radiation is directed close to the axis of the device. Like a bending magnet, wigglers produce a continuous spectrum but with the critical energy shifted to harder energies because the magnetic field is (usually) greater. Thus for a wiggler at a 6-GeV source, with a magnetic field of 1.2 T and a magnetic period of 125 mm, K is 14, the maximum deflection of the electrons from the straight-line path is 1.2 mrad and the critical photon energy is 28.7 keV. Magnetic fields of several tesla can be exploited using superconducting magnets to obtain even higher critical photon energies.

2.2.2.2.2. *Undulators*

If the value of K is 2 or less, the insertion device is an undulator. The deflection of the electrons is comparable to the natural opening angle of the emitted radiation $1/\gamma$. Radiation emitted from sequential oscillations interferes coherently, and the beam

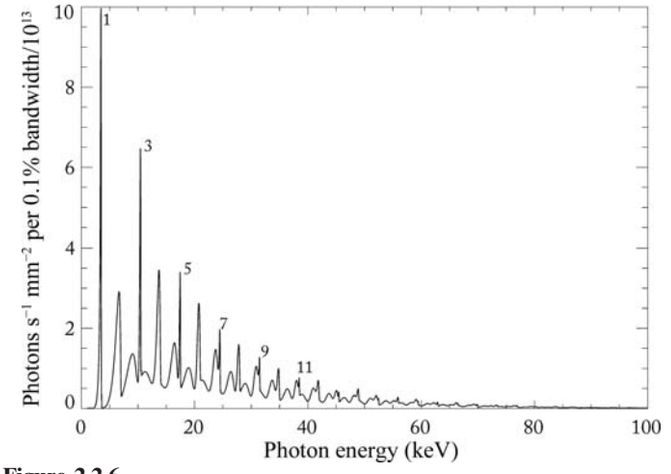

Figure 2.2.6
Photon flux *versus* energy through a 1-mm^2 aperture 30 m from the source, 0.1% bandwidth, for an ESRF u35 undulator (magnetic periodicity 35 mm, 1.6 m long, magnetic gap of 11 mm, peak magnetic field B_0 = 0.71 T, electron energy 6 GeV, K = 2.31, storage-ring current 200 mA). Odd-numbered harmonics are labelled, which are those usually employed for powder-diffraction experiments as they have maximum intensity on axis.

becomes highly collimated in the horizontal and vertical directions. Thus, the radiation from an undulator is concentrated into a central on-axis cone (fundamental and odd harmonics), surrounded by rings from higher-order even harmonics. The flux density arriving on a small sample from this central cone is therefore very high. With high on-axis intensity, it is therefore the undulators that provide the beams with the highest spectral brightness at any synchrotron-radiation source. The interference also modifies the spectrum of the device, which has a series of harmonics derived from a fundamental energy. At a horizontal angle θ to the axis of the insertion device, the wavelength of harmonic n is given by

$$\lambda_n = \frac{1 + (K^2/2) + \gamma^2\theta^2}{2n\gamma^2}\lambda_u,$$

which can be simplified on axis ($\theta = 0$) to

$$\lambda_n\ [\text{Å}] = 1.3056\frac{1 + K^2/2}{nE_e^2\ [\text{GeV}]}\lambda_u\ [\text{mm}]$$

or

$$\varepsilon_n\ [\text{keV}] = 9.50\frac{nE_e^2\ [\text{GeV}]}{\lambda_u\ [\text{mm}](1 + K^2/2)}.$$

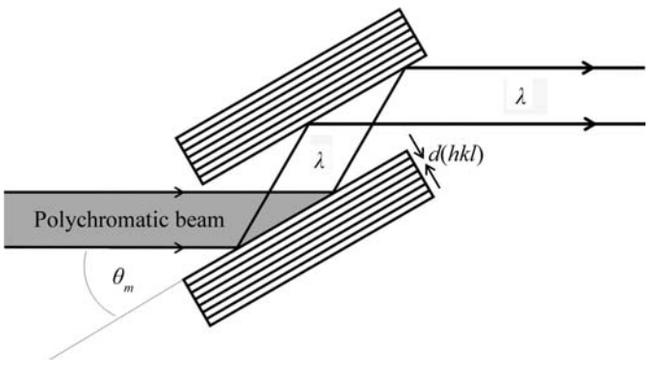

Figure 2.2.7
Double-crystal monochromator arrangement.

On axis, only odd-numbered harmonics are emitted and it is these that are usually employed in a powder-diffraction experiment. The horizontal and vertical divergence of the radiation emerging from an undulator is of the order of $1/[(nN)^{1/2}\gamma]$, where N is the number of magnetic periods making up the device. The spectrum of an undulator at a 6-GeV source with a 35-mm magnetic period is shown in Fig. 2.2.6. By carefully shimming the magnetic lattice so that it is highly regular, the higher-order harmonics persist, allowing the undulator to be a powerful source of high-energy X-rays. Any imperfections in the magnetic periodicity cause the higher-order harmonics to broaden and fade away, reducing the utility of the device at higher energies.

2.2.2.2.3. *Tuning*

For insertion devices the magnetic field can be modified by changing the vertical distance between the magnetic poles. By opening the gap, the magnetic field and K decrease following

$$B_0 \simeq B_r \exp(-\pi G/\lambda_u),$$

where B_r is proportional to the remanent magnetic field, which depends upon the nature of the magnets used in the insertion device, and G is the magnetic gap. Decreasing K for an undulator means that the energy of the fundamental harmonic increases; however, this is at the expense of the intensities of the higher harmonics. Thus the insertion device can be tuned to produce high intensity at the wavelength most suitable for a particular measurement. The smallest gap possible for a device depends on the design of the storage-ring vacuum vessel in which the electrons circulate. It is difficult to have a vessel smaller than about 10 mm high, and hence for an externally applied field a minimum magnetic gap of about 11 mm is to be expected. For smaller gaps, the magnets must be taken into the vacuum of the storage ring, a so-called 'in-vacuum' insertion device.

2.2.3. Optics

The intense polychromatic beam from the source needs to be conditioned before hitting the sample and diffracting. In the simplest experimental configuration, the white beam is used in an energy-dispersive experiment, and conditioning may involve no more than using slits to define the horizontal and vertical beam sizes and suppress background scattering. More usually, monochromatic radiation is employed, and the desired wavelength is chosen from the source by a monochromator. A monochromator consists of a perfect crystal, or a pair of crystals, set to select the chosen wavelength by Bragg diffraction. Additional optical elements can also be incorporated into the beamline for focusing, collimation, or for filtering out unwanted photons to reduce heat loads or remove higher-order wavelengths transmitted by the monochromator.

2.2.3.1. *Monochromator*

The monochromator is a crucial optical component in any angle-dispersive powder-diffraction beamline, and consists of one or a pair of perfect crystals (*e.g.* Beaumont & Hart, 1974), Fig. 2.2.7, set to a particular angle to the incident beam, θ_m, that transmits by diffraction wavelengths that satisfy the Bragg equation, $n\lambda = 2d(hkl)\sin\theta_m$, where $d(hkl)$ is the lattice spacing of the chosen reflection. Note that photons from higher-order reflections can also be transmitted, corresponding to wavelengths λ/n, depending on the structure factor of the nth-order reflection and its Darwin width, but these can be eliminated by use of a

mirror (see Section 2.2.3.2), or by adjusting the electronic acceptance windows of the detector system, if possible. They can also be suppressed to some extent by slightly detuning the second crystal from the first, because the Darwin width of a higher-order reflection is narrower than that of a lower-order reflection, and is thus more seriously affected by the mismatch between Bragg angles.

For a given reflection, a crystal does not transmit a unique single wavelength but a narrow distribution. The width of the distribution, $\delta\lambda$, is determined by the effective divergence of the incident beam Ψ (which corresponds to a range of values for θ_m) and the Darwin width of the reflection, ω, at the chosen wavelength. The energy resolution of a monochromator crystal can be estimated *via*

$$\delta\varepsilon/\varepsilon = \delta\lambda/\lambda = \cot\theta_m(\Psi^2 + \omega^2)^{1/2}.$$

With a highly collimated beam incident on a crystal and with a narrow Darwin width, high energy resolution is achieved. The Darwin width of a reflection can be calculated from dynamical theory [Zachariasen (1945); Chapter 5.1 of *International Tables for Crystallography*, Volume B (Authier, 2006)] *via*

$$\omega = \frac{2r_e\lambda^2}{\pi V}|F(\mathbf{h})|\frac{K}{\sin 2\theta_m},$$

where r_e is the classical electron radius ($\sim$2.818 fm), V is the volume of the unit cell, $F(\mathbf{h})$ is the structure factor and K the polarization factor (1 for reflection in the vertical plane, $\cos 2\theta_m$ for the horizontal plane). Thus for Si(111), with $d(111)$ = 3.1356 Å and $F(\mathbf{h}) \simeq 59$, a Darwin width of about 8.3 µrad is obtained at 31 keV (λ = 0.4 Å). With an effective beam divergence of say 25 µrad (delivering a beam 1.1 mm high at 44 m from the source), an energy resolution of 4.8×10^{-4} is obtained. Even better energy resolution can be obtained by increasing the collimation of the beam before the monochromator, *e.g.* with a curved mirror.

Energy resolution is an important quantity to control. Its value needs to be known when modelling powder-diffraction peak shapes *via* a fundamental-parameters approach, and it affects the angular resolution of the powder-diffraction pattern, broadening the peaks as 2θ increases, as can be seen by differentiating the Bragg equation to yield

$$\frac{\delta\lambda}{\lambda} = \cot\theta\,\delta\theta \quad \text{or} \quad \delta\theta = \frac{\delta\lambda}{\lambda}\tan\theta. \tag{2.2.1}$$

Thus powder-diffraction peaks broaden towards higher 2θ angles because of this effect.

Silicon is a common choice for a monochromator; it forms large, perfect single crystals, with dimensions of cm if required, has appropriate mechanical, diffraction and thermal properties, and can resist prolonged exposure to an intense radiation source. A monochromator crystal absorbs a large fraction of the energy incident upon it, and hence must be cooled. Even when cooled, the high power density (tens or even more than a hundred W mm^{-2} at normal incidence) can cause local heating of the surface, which leads to distortion of the lattice planes *via* thermal expansion. This degrades the performance, as a heat bump increases the range of θ_m values, broadening the energy band transmitted by the crystal. With a double-crystal arrangement, this bump cannot be matched by the second crystal, which has a much lower heat load so is flat, with the result that photons from the first crystal are not transmitted by the second, thus losing intensity from the monochromatic beam. By cooling to cryogenic temperatures, the thermal expansion of Si can be reduced to a very small value, going through zero at around 120 K (Bilderback, 1986; Glazov & Pashinkin, 2001) and thereby alleviating the heat-bump problem. Thus cryogenically cooled monochromators can be found at high-performance synchrotron beamlines. Other crystals employed as monochromators are germanium and diamond, the latter in transmission because of the small size of available diamond crystals.

Although a monochromator assembly can employ only one crystal, for example deflecting the beam horizontally into a side branch of a beamline, a double-crystal arrangement (Fig. 2.2.7) is more usually used to conserve the direction of the beam from the storage ring. This can exploit either a channel-cut crystal or two crystals, with a number of adjustments in the position and orientation of the second crystal to allow it to be aligned optimally to transmit the wavelength envelope defined by the first crystal. In some cases, the second crystal can be bent sagittally to focus X-rays horizontally onto the sample. Although this increases the divergence of the beam arriving at the sample and so affects the 2θ resolution of the powder pattern, it can lead to a significant increase in intensity, and is useful to capture more radiation from a horizontally divergent source such as a bending magnet or wiggler.

2.2.3.2. *Mirror*

Some powder-diffraction beamlines are equipped with X-ray mirrors, which can be used to focus or to improve the collimation of the already highly collimated beam, and to act as a high-energy filter for photons with energies above a certain value, *e.g.* to remove higher-order wavelengths transmitted by the monochromator. Usually reflecting in the vertical plane, a mirror consists of a highly polished substrate (*e.g.* Si) with a thin metal coating, such as Pt or Rh, set at grazing incidence. The nature of the coating and the graze angle determine the energy cutoff, where the reflectivity falls to very low values following

$$\theta_c\ [\text{mrad}] = 2.324(\rho Z/A)^{1/2}\lambda\ [\text{Å}],$$

where θ_c is the critical graze angle for X-rays of wavelength λ, ρ is the density, Z is the atomic number and A is the atomic weight of the metal coating. As an example, an Rh-coated mirror set at a grazing incidence of 2 mrad will only reflect X-rays with a wavelength longer than around 0.37 Å. A Pt-coated mirror set at the same graze angle will transmit shorter wavelengths, down to 0.30 Å. The wavelength cutoff for a particular mirror can be adjusted by changing the angle of grazing incidence. However, this then entails realignment of the beamline downstream of the mirror. To avoid this, some beamlines have mirrors with stripes of different metals, allowing adjustment of the cutoff by simply translating the mirror sideways to change the coating while keeping the graze angle constant.

Curving a mirror concavely as shown in Fig. 2.2.8 allows focusing or collimation, following

$$R = \frac{2L_1L_2}{(L_1 + L_2)\sin\alpha},$$

where R is the radius of curvature, L_1 is the source-to-mirror distance, L_2 is the mirror-to-focus distance and α is the angle of grazing incidence. For collimation ($L_2 = \infty$), this reduces to $R = 2L_1/\sin\alpha$. Thus a mirror 25 m from the source set at a graze angle of 2 mrad must be curved to a radius of 25 km to collimate the beam. As noted above, silicon is frequently chosen as a substrate for a mirror as it is sufficiently stiff to help minimize the intrinsic

Figure 2.2.8
Curved mirror set to collimate the beam.

curvature of the mirror caused by its own weight. Even then, very careful mounting and precise mechanics are required to achieve this level of accuracy. If placed in the polychromatic beam directly from the source, cooling of the mirror will be necessary.

Other mirror arrangements can be employed, such as a horizontal and vertical pair of focusing mirrors in a Kirkpatrick–Baez (Kirkpatrick & Baez, 1948) arrangement. Such a device might be used to produce a small focal spot for powder-diffraction measurements from a sample in a diamond anvil cell. Multilayer mirrors can also be found in service on certain beamlines.

2.2.3.3. *Compound refractive lens*

The refractive index n of a material for X-rays is given (Gullikson, 2001; Spiller, 2000) by

$$n = 1 - \delta - i\beta = 1 - \frac{r_e}{2\pi}\lambda^2 \sum_n N_n f_n,$$

where $f_n = f_1 + if_2$ is the complex scattering factor for forward scattering for atom n and N_n is the number of atoms of type n per unit volume. δ and β are known as the refractive index decrement and the absorption index, respectively, and vary with photon energy depending on the proximity of an absorption edge. The real part of the refractive index is therefore slightly less than 1, with δ typically of the order 10^{-6}–10^{-9} depending on the energy. Thus a hole drilled in a piece of metal can act like a conventional convex lens, as the hole has a higher refractive index than the surrounding metal. With such a small difference in n between hole and metal, the focusing power is very slight; however, a series of holes (Fig. 2.2.9) can be used to focus the X-ray beam over a reasonable distance (Snigirev *et al.*, 1997, 1998). For a series of cylindrical lenses, the focal length, f, is given by $f = r/2N\delta$, where r is the radius of the hole and N is the number of holes.

Note that further away from the axis of the device the X-ray beam must pass through increasing amounts of material which absorb the radiation. Hence, only relatively small holes and apertures are possible (a maximum of a few mm in diameter) and weakly absorbing metals such as Be and Al are preferred. With hard-energy photons, Ni lenses are possible, and indeed the construction of such a device is a compromise between refractive power, absorption, aperture and the desired focal length. Such devices can be placed in the monochromatic beam or in a polychromatic beam with cooling.

Many variants of the basic scheme exist, with lenses pressed from foil with a parabolic form to eliminate spherical aberrations, with axial symmetry to focus in both the horizontal and vertical simultaneously (Lengeler *et al.*, 1999), etched *via* lithography from plastic or other material, or with a more complex profile to minimize the amount of redundant material attenuating the transmitted beam by absorption and so allowing a larger aperture. A 'transfocator' can be constructed whereby series of lenses can be accurately inserted or removed from the beam path, thus allowing the focusing power to be adjusted depending on the

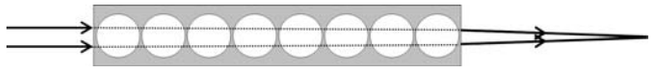

Figure 2.2.9
Schematic diagram of a set of refractive lenses.

desired focal distance and the wavelength of the experiment (Vaughan *et al.*, 2011).

2.2.4. Diffractometers

Most powder-diffraction beamlines are angle dispersive, operating with monochromatic radiation. When scanning a detector arm or employing a curved position-sensitive detector (PSD), detection is normally in the vertical plane because the polarization of the radiation in the plane of the synchrotron orbit means there is very little effect on the intensities due to polarization. By contrast, if diffracting in the horizontal plane, the projection of the electric vector onto the direction of the diffracted beam means that the intensity is reduced by a factor of $\cos^2 2\theta$, going to zero at $2\theta = 90°$, and so horizontal detection is less useful unless working at hard energies when 2θ angles are correspondingly small. In addition, for the highest angular resolution, the natural beam divergence in the vertical plane is usually lower than in the horizontal plane, particularly if the instrument has a bending magnet or wiggler as its source.

In general, diffractometers are heavy-duty pieces of equipment and are designed to have excellent angular accuracy while working with substantial loads. A high degree of mechanical accuracy is required to match the high optical accuracy inherent in the techniques employed. The calibration of the incident wavelength and any 2θ zero-point error is best done by measuring the diffraction pattern from a sample such as NIST standard Si (640 series), each of which has a certified lattice parameter (see Chapter 3.1). It is also good practice to measure the diffraction pattern of a standard sample regularly and whenever the instrument is realigned or the wavelength changed, to be sure that everything is working as expected.

Monochromatic instruments can have an analyser crystal or long parallel-foil collimators in the diffracted beam (a so-called parallel-beam arrangement), or can scan a receiving slit, or possess a one- or two-dimensional PSD, similar to Debye–Scherrer or Laue front-reflection geometry. Instruments equipped with a PSD can collect data much faster than those with a scanning diffractometer, so are exploited especially for time-resolved measurements. They may also have advantages for rapid data collection if the sample is sensitive to radiation, or be helpful if the sample is prone to granularity or texture to assess the extent of the problem.

Instruments can also be equipped with a sample changer, allowing measurements on a series of specimens, perhaps prepared by systematically changing the conditions of synthesis or the composition in a combinatorial approach. The use of beam time can be optimized with minimal downtime due to interventions around the instrument, and with the possibility to control the data acquisition remotely if desired.

2.2.4.1. *Parallel-beam instruments*

Cox *et al.* (1983, 1986), Hastings *et al.* (1984) and Thompson *et al.* (1987) described the basic ideas behind these instruments *via* their pioneering work at CHESS (Cornell, USA) and NSLS (Brookhaven, USA). The highly collimated monochromatic

incident beam is diffracted by the sample and passes *via* a perfect analyser crystal [such as Si or Ge(111)] to the detector. The analyser crystal defines a very narrow angular acceptance for the diffracted radiation, determined by its Darwin width. The combination of the collimation of the incident radiation, its highly monochromatic nature and the stringent angular acceptance defines the instrument's excellent angular resolution. The detector arm supporting the analyser is scanned through the desired range of 2θ angles either in a step-scan mode or continuously, reading out at very short intervals the electronic modules that accumulate the detector counts.

To be transmitted by the analyser crystal, a photon must be incident on the crystal at the correct angle θ_a that satisfies the Bragg condition. The analyser crystal defines therefore a true direction (2θ angle) for the diffracted beam irrespective of where in the sample it originates from. This removes a number of aberrations that affect diffractometers with a scanning slit or PSD where the 2θ angle is inferred from the position of the slit or detecting pixel. Thus, with a capillary specimen, peak widths are independent of the capillary diameter, so a fat capillary of non-absorbing sample can be used to optimize diffracted intensity, and any modest misalignment of the sample from the diffractometer axis, or specimen transparency or surface roughness for flat-plate samples, does not lead to shifts in the peak positions. Modest movement of the sample with temperature changes in a furnace *etc*. does not cause shifts in peak positions. These instruments are therefore highly accurate, and are ideal for obtaining peak positions for indexing a diffraction pattern of a material of unknown unit cell (the first step in the solution of a structure from powder data), or following the evolution of lattice parameter with temperature *etc*. For flat samples, the $\theta/2\theta$ parafocusing condition does not need to be satisfied to have high resolution. The peak width does not therefore depend on sample orientation, which is useful for measurements of residual strain by the $\sin^2\psi$ technique or for studying surfaces and surface layers by grazing-incidence diffraction. Interchange between capillary and flat-plate samples can easily be done as required without major realignment of the instrument. The stringent acceptance conditions also help to suppress parasitic scattering originating from sample-environment windows *etc*. and inelastic scattering such as fluorescence and Compton scattering.

On the other hand, at any 2θ angle only a tiny fraction of the diffracted photons can be transmitted by an analyser crystal, so this is a technique that consumes a lot of photons, and the high incident flux is essential to keep scan times to reasonable values. To overcome this, at least to some extent, Hodeau *et al.* (1998) devised a system of multiple analyser crystals, with nine channels mounted in parallel, each separated from the next by 2° (Fig. 2.2.10). In effect, as the detector arm is scanned, nine high-resolution powder-diffraction patterns are measured in parallel, each offset from the next by 2°. If the data from the channels are to be combined, which is the usual procedure, the detectors must be calibrated with respect to each other, in terms of counting efficiency and exact angular offset, by comparing regions of the diffraction pattern scanned by several detectors (Wright *et al.*, 2003). A multianalyser system speeds up data collection significantly and can be found in various modified forms at a number of powder-diffraction beamlines (*e.g.* Lee, Shu *et al.*, 2008).

The multianalyser approach is best suited to capillary samples because of the axial symmetry of the arrangement. With flat plates in reflection, only one detector can be in the $\theta/2\theta$ condition where the effect of specimen absorption (for a sufficiently thick sample) is isotropic. Corrections must therefore be made to the intensities from the other channels (Lipson, 1967; Koopmans & Rieck, 1968). For a capillary, choosing the wavelength and the diameter allows absorption to be kept to an acceptable value. Maximum diffracted intensity is expected at $\mu r = 1$ (where μ is the linear absorption coefficient and r the radius of the capillary), and below this value simple absorption corrections can be applied (Hewat, 1979; Sabine *et al.*, 1998). A value of μr greater than 1.5 begins to degrade the quality of the pattern significantly. If a sample with high absorption is unavoidable, such as when working close to an absorption edge of an element, *e.g.* the *K* edge of Mn at 6.539 keV (1.896 Å), then it can be preferable to stick a thin layer of sample on the outside of a 1-mm-diameter capillary. The shell-like nature of the sample has no effect on the peak shape or resolution because of the use of analyser crystals.

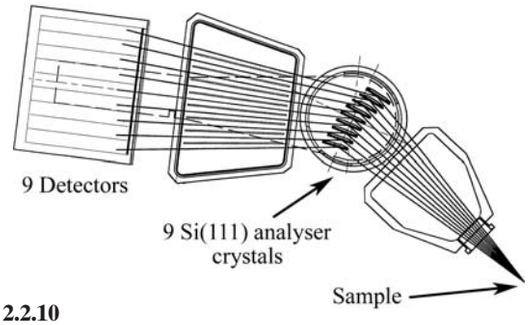

Figure 2.2.10
Multianalyser stage, nine channels separated by 2°, devised by Hodeau *et al.* (1998), originally installed on the BM16 bending-magnet beamline at the ESRF with Ge(111) analyser crystals. With an undulator source, the greatly increased flux allows use of Si(111), which has a narrower Darwin width (by a factor of ∼2.4) and thus improved 2θ resolution, but with a lower fraction of the diffracted radiation accepted.

Capillaries also have the advantage that preferred orientation can be significantly less as compared to a flat sample, where there is a tendency for crystallites to align in the surface layers, especially if compressed to hold the powder in place. Spinning or otherwise moving the sample is necessary, whether capillary or flat plate, to increase the number of crystallites appropriately oriented to fulfil the Bragg condition and avoid a spotty diffraction pattern, the likelihood of which is exacerbated by the highly collimated nature of the incident radiation.

2.2.4.1.1. *Angular resolution*

Various authors (*e.g.* Sabine, 1987*a*,*b*; Wroblewski, 1991; Masson *et al.*, 2003; Gozzo *et al.*, 2006) have discussed the resolution of a synchrotron-based diffractometer equipped with a double-crystal monochromator and an analyser crystal. The most usual setting of the diffracting crystals, ignoring any mirrors or other optical devices, is non-dispersive, alternatively described as parallel or (1, −1, 1, −1).

The approach developed by Sabine (1987*a*,*b*) involves modelling the vertical divergence of the source and the angular acceptance of the monochromator and analyser crystals as Gaussian distributions with the same full width at half-maximum (FWHM) as the real distributions, and considering a powder as a crystal with an infinite mosaic spread. The rocking curve of the analyser crystal (equivalent to rocking 2θ) is given by

$$I(\beta) = \int\int \mathrm{d}\alpha\,\mathrm{d}\delta \exp\left\{-\left[\left(\frac{\alpha}{\alpha'_m}\right)^2 + 2\left(\frac{\delta-\alpha}{\Delta'_m}\right)^2 + \left(\frac{b\delta+\alpha-\beta}{\Delta'_a}\right)^2\right]\right\},$$

where

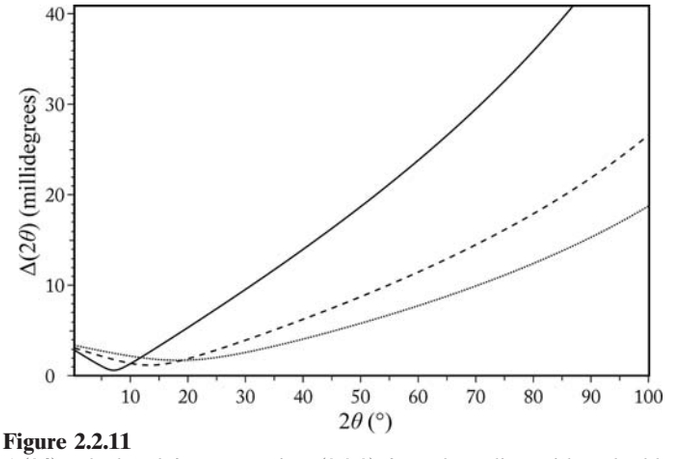

Figure 2.2.11
$\Delta(2\theta)$ calculated from equation (2.2.2) for a beamline with a double-crystal Si(111) monochromator, an Si(111) analyser ($\Delta_m = \Delta_a$ and $\theta_m = \theta_a$) and an FWHM vertical divergence of 25 μrad at $\lambda = 0.4$ Å (solid line: $\Delta_m \simeq 8.3$ μrad, $\theta_m = 3.6571°$), $\lambda = 0.8$ Å (dashed line: $\Delta_m \simeq 16.6$ μrad, $\theta_m = 7.3292°$) and $\lambda = 1.2$ Å (dotted line: $\Delta_m \simeq 25.2$ μrad, $\theta_m = 11.0319°$).

$$b = \tan\theta_a/\tan\theta_m - 2\tan\theta/\tan\theta_m.$$

Here α represents the vertical divergence from the source, δ is the difference between the Bragg angles of a central ray reflected from the monochromator at the angle θ_m and of another ray at angle θ'_m such that $\delta = \theta'_m - \theta_m$, and θ_a is the Bragg angle of the analyser crystal. The terms α'_m, Δ'_m and Δ'_a are related to the FWHM of the Gaussians representing the vertical divergence distribution or the Darwin widths of the monochromator and analyser crystals, α_m, Δ_m and Δ_a, respectively, with

$$\alpha'_m = \alpha_m/2(\ln 2)^{1/2}, \quad \Delta'_m = \Delta_m/2(\ln 2)^{1/2}, \quad \Delta'_a = \Delta_a/2(\ln 2)^{1/2}.$$

From the above equation, the intrinsic FWHM of the Gaussian-approximated peaks of the powder-diffraction pattern can be obtained as

$$\Delta^2(2\theta) = \alpha_m^2\left(\frac{\tan\theta_a}{\tan\theta_m} - 2\frac{\tan\theta}{\tan\theta_m} + 1\right)^2 + \tfrac{1}{2}\Delta_m^2\left(\frac{\tan\theta_a}{\tan\theta_m} - 2\frac{\tan\theta}{\tan\theta_m}\right) + \Delta_a^2. \quad (2.2.2)$$

Note that the true peak shape is not Gaussian, and a pseudo-Voigt (*e.g.* as described by Thompson *et al.*, 1987), Voigt (*e.g.* Langford, 1978; David & Matthewman, 1985; Balzar & Ledbetter, 1993) or other function modelled from first principles (*e.g.* Cheary & Coelho, 1992; Ida *et al.*, 2001, 2003) is usually better. Examples of FWHM curves calculated from equation (2.2.2) are plotted in Fig. 2.2.11 at three wavelengths. Differentiating the Bragg equation gives $\Delta d/d = -\cot\theta\,\Delta(\theta)$, where θ is in radians.

Gozzo *et al.* (2006) have extended the formulation of Sabine to include the effects of collimating and focusing mirrors in the overall scheme. Axial (horizontal) divergence of the beam between the sample and the detector causes shifts and broadening of the peaks, as well as the well known low-angle peak asymmetry due to the curvature of the Debye–Scherrer cones. Sabine (1987*b*), based on the work of Hewat (1975) and Hastings *et al.* (1984), suggests the magnitude of the broadening, $B(2\theta)$, due to horizontal divergence Φ can be estimated *via*

$$B(2\theta) = (\tfrac{1}{4}\Phi)^2(\cot 2\theta + \tan\theta_a),$$

where B and Φ are in radians. This value is added to $\Delta(2\theta)$.

2.2.4.1.2. *Hart–Parrish design*

A variant of the parallel-beam scheme replaces the analyser crystal with a set of long, fine Soller collimators (Parrish *et al.*, 1986; Parrish & Hart, 1987; Parrish, 1988; Cernik *et al.*, 1990; Collins *et al.*, 1992) (Fig. 2.2.12). The collimators define a true angle of diffraction, but with lower 2θ resolution than an analyser crystal because their acceptance angle is necessarily much larger and so the transmitted intensity is greater. They are not particularly suitable for fine capillary specimens, as the separation between foils may be similar to the capillary diameter, resulting in problems of shadowing of the diffracted beam. However, they are achromatic, and so do not need to be reoriented at each change of wavelength, which may have advantages when performing anomalous-scattering studies around an element's absorption edge. Unlike an analyser crystal, however, they do not suppress fluorescence. Peak shapes and resolution can be influenced by reflection of X-rays from the surface of the foils, or any imperfections in their manufacture, *e.g.* if the blades are not straight and flat. The theoretical resolution curve of such an instrument can be obtained from equation (2.2.2) by setting $\tan\theta_a$ to zero and replacing the angular acceptance of the analyser crystal Δ_a with the angular acceptance of the collimator Δ_c.

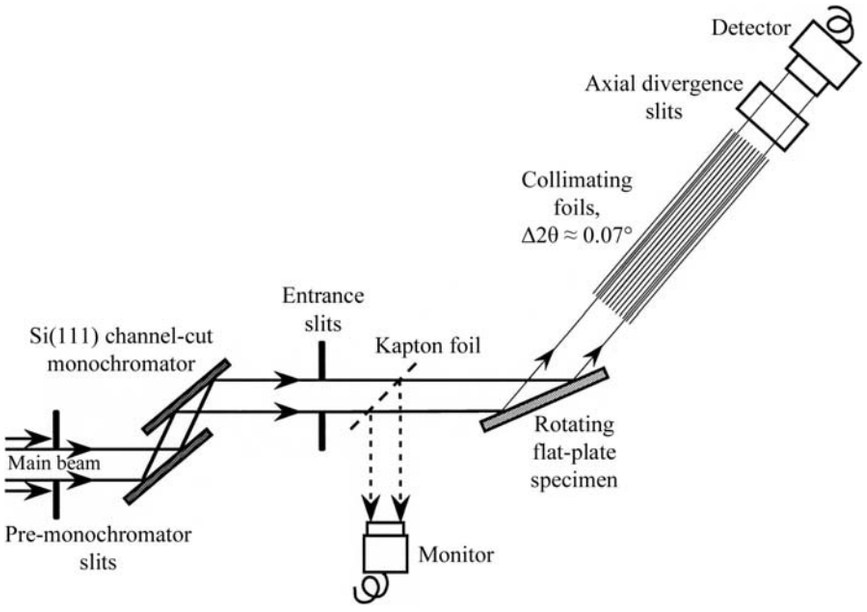

Figure 2.2.12
Schematic representation of a parallel-beam diffractometer of the Hart–Parrish design. The collimators installed on Stations 8.3 and 2.3 at the SRS Daresbury (Cernik *et al.*, 1990; Collins *et al.*, 1992) had steel blades 50 μm thick, 355 mm long, separated by 0.2 mm spacers, defining a theoretical opening angle (FWHM Δ_c) of 0.032° and a transmission of 80%.

2.2.4.2. *Debye–Scherrer instruments*

The simplest diffractometer has a receiving slit at a convenient distance from the sample in front of a point detector such as a scintillation counter. The height of the slit should match the capillary diameter, or incident beam height for flat plates. A slightly larger antiscatter slit near the sample should also be employed to reduce

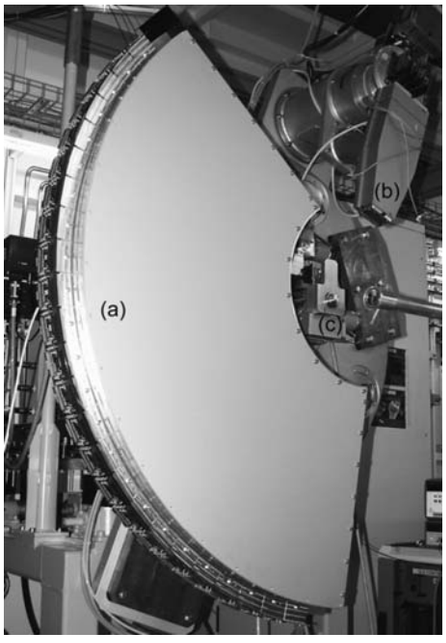

Figure 2.2.13
(*a*) 120° Mythen detector box, containing helium, mounted on the powder diffractometer of the materials science beamline at the Swiss Light Source. (*b*) Multianalyser detector stage. (*c*) Capillary spinner. (Bergamaschi *et al.*, 2009, 2010.)

background. The detector arm is scanned and a powder pattern recorded. This arrangement can be used for narrow capillary samples on lower-flux sources, avoiding the loss of intensity that use of an analyser crystal entails. The resolution is largely determined by the opening angle defined by the capillary and the receiving slit. Despite the simplicity of such an instrument, high-quality high-resolution data can be obtained.

For much faster data acquisition, a one-dimensional (1D) PSD or an area detector can be employed. Any sort of 1D detector with an appropriate number of channels, channel separation, efficiency, count rate (in an individual channel and overall) and speed of read out can be employed. Technology evolves and detectors make continual progress in performance. At the time of writing the most advanced 1D detector is the Mythen module developed by the Swiss Light Source (SLS). Mythen modules are based on semiconducting silicon technology and have 1280 8-mm-wide strips with a 50 μm pitch (64 × 8 mm^2). They can be combined to form very large curved detectors such as that on the powder diffractometer of the materials science beamline at the SLS (Fig. 2.2.13). This detector consists of 24 modules, 30 720 channels, set on a radius of 760 mm, covering 120° 2θ. Detector elements are therefore separated by ∼0.004°. The whole detector can be read out in 250 μs. Being Si based, its efficiency falls off above 20–25 keV, where the absorbing power of Si falls to very small values. Nevertheless, at intermediate and low energies a full powder-diffraction pattern for structural analysis can be measured in just seconds, or even faster if the intention is to follow a dynamic process.

Two-dimensional (2D) detectors are generally flat, so cannot extend to the same 2θ values as a curved multistrip detector unless scanned on a detector arm. This is possible, but usually a short wavelength is used with a fixed detector. This allows an adequate data range to be recorded, particularly if the detector is positioned with the direct beam ($2\theta = 0$) near an edge. A 2D detector records complete or partial Debye–Scherrer rings, which increases the counting efficiency with respect to scanning an analyser crystal by several orders of magnitude. In addition, if the rings do not appear smooth and homogeneous, this indicates problems with the sample, such as preferred orientation or granularity, both of which can seriously affect diffraction intensities when measuring just a thin vertical strip. Detectors that have been used are diverse and include image plates, though these have slow read out, charge-coupled devices (CCDs) or Si-based photon-counting pixel detectors used for single-crystal diffraction or protein crystallography (*e.g.* Broennimann *et al.*, 2006), and medical-imaging detectors, which are designed for hard-energy operation. Examples include the CCD-based Frelon camera, developed at the ESRF (Labiche *et al.*, 2007), and commercially available large flat-panel medical-imaging detectors up to 41 × 41 cm^2, based on scintillator-coated amorphous silicon, which have been exploited at speeds of up to 60 Hz for selected read-out areas (Chupas, Chapman & Lee, 2007; Lee, Aydiner *et al.*, 2008; Daniels & Drakopoulos, 2009).

Note that a 2D detector can be used as a 1D detector by applying a mask and reading out only a narrow strip, which can enhance the rate of data acquisition. For CCD chips, the electronic image can be rapidly transferred to pixels behind the masked part of the detector from where it can be read out while the active area is re-exposed. Translating an image plate behind a mask is a simple way of acquiring a series of diffraction patterns for following a process with modest time resolution.

These instruments are vulnerable to aberrations that cause systematic shifts in peak positions, such as misalignment of the capillary or surface of the sample from the diffractometer axis, and specimen transparency, which also affects the peak width and shape. The peak width also depends on whether a flat sample is in the $\theta/2\theta$ condition, or on the diameter of a capillary sample, *etc*. Focusing the incident beam onto the detector decreases the peak width, as fewer pixels are illuminated compared to using a highly collimated incident beam. PSDs are much more open detectors than those behind an analyser crystal or set of slits, so are more susceptible to background and parasitic scatter from sample environments *etc*. However, the speed and efficiency of data acquisition usually outweigh such concerns.

2.2.4.3. *Energy-dispersive instruments*

The broad, continuous spectrum from a wiggler or bending magnet is suitable for energy-dispersive diffraction (EDD). Here, the detector is fixed at an angle 2θ and the detector determines the energy, ε, of each arriving photon scattered by the sample (Fig. 2.2.14). The energy [keV] can be converted to d-spacing [Å] *via*

$$d \simeq 12.3984/2\varepsilon \sin\theta.$$

The detector usually consists of a cryogenically cooled semiconducting Ge diode. An absorbed X-ray photon promotes electrons to the conduction band in proportion to its energy. By

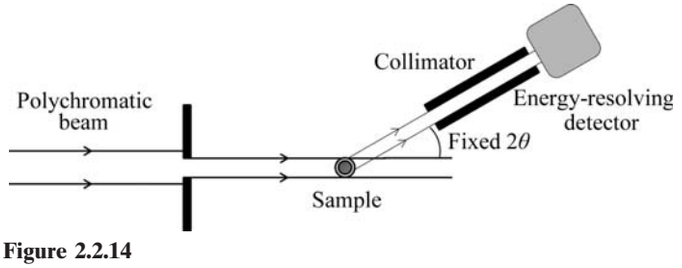

Figure 2.2.14
Schematic representation of an energy-dispersive diffraction arrangement.

analysing the size of the charge pulse produced, the energy of the photon is determined. The powder-diffraction pattern is recorded as a function of energy (typically somewhere within the range 10–150 keV, depending on the source) *via* a multichannel analyser (MCA). Instruments may have multiple detectors, at different 2θ angles covering different ranges in d-spacing (Barnes *et al.*, 1998), or arranged around a Debye–Scherrer ring, as in the 23-element semi-annular detector at beamline I12 at Diamond Light Source (Korsunsky *et al.*, 2010; Rowles *et al.*, 2012).

Prior to performing the EDD experiment, the detector and MCA system must be calibrated, *e.g.* by measuring signals from sources of known energy, such as ^{241}Am (59.5412 keV) or ^{57}Co (122.06014 and 136.4743 keV) at hard energies, and/or from the fluorescence lines of elements such as Mo, Ag, Ba *etc*. The 2θ angle also needs to be calibrated if accurate d-spacings are desired. This should be done by measuring the diffraction pattern of a standard sample with known d values.

The detector angle is typically chosen in the range 2–6° 2θ and influences the range of d-spacings accessible *via* the term $1/\sin\theta$, *i.e.* the lower the angle, the higher the energy needed to access any particular d. Normally, the range of most interest should be matched to the incident spectrum, taking account also of sample absorption and fluorescence, to produce peaks with high intensity. More than one detector at different angles can also be employed. Energy-sensitive Ge detectors do not count particularly fast, up to 50 kHz being a typical value compared to possibly 1–2 MHz with a scintillation detector. Hence they are relatively sensitive to pulse pile-up and other effects of high count rates (Cousins, 1994; Laundy & Collins, 2003; Honkimäki & Suortti, 2007), particularly if the synchrotron is operating in a mode with a few large electron bunches giving very intense pulses of X-rays on the sample.

The energy resolution of the detector is of the order of 2%, which dominates the overall resolution of the technique. Its main uses are where a fixed geometry with penetrating X-rays is required, *e.g.* in high-pressure cells, for *in situ* studies (Häusermann & Barnes, 1992), *e.g.* of chemical reactions under hydrothermal conditions (Walton & O'Hare, 2000; Evans *et al.*, 1995), electrochemistry (*e.g.* Scarlett *et al.*, 2009; Rijssenbeek *et al.*, 2011; Rowles *et al.*, 2012), or measurements of residual strain (Korsunsky *et al.*, 2010). Owing to the use of polychromatic radiation, the technique has very high flux on the sample and can be used for high-speed data collection, following rapid processes *in situ*. However, accurate modelling of the intensities of the powder-diffraction pattern for structural or phase analysis is difficult because of the need to take several energy-dependent effects into account, *e.g.* absorption and scattering factors, the incident X-ray spectrum, and the detector response. Nevertheless, examples where this has been successfully carried out have been published (*e.g.* Yamanaka & Ogata, 1991; Scarlett *et al.*, 2009).

A higher-resolution variant of the energy-dispersive technique can be performed by using a standard detector behind a collimator at fixed 2θ scanning the incident energy *via* the monochromator. The Hart–Parrish design with long parallel foils is suitable. Such an approach has been demonstrated in principle (Parrish, 1988), but is rarely used in practice. The advantage is to be able to measure data of improved d-spacing resolution, as compared to using an energy-dispersive detector, from sample environments with highly restricted access. In principle, as a further variant, white incident radiation could be used with scanning of θ_a, the angle of the analyser crystal, and associated detector at $2\theta_a$, all at fixed 2θ.

2.2.5. Considerations for powder-diffraction experiments

Synchrotron radiation allows considerable flexibility for a powder-diffraction experiment, offering choice and optimization of a number of quantities such as the wavelength, with high energy resolution, range in d-spacing, angular resolution, angular accuracy, and spatial or time resolution (but not all of these can necessarily be optimized at the same time). Increasingly, powder-diffraction experiments at synchrotrons are combined with complementary measurements, simultaneously applying techniques such as Raman spectroscopy (Boccaleri *et al.*, 2007; Newton & van Beek, 2010), particularly when carrying out *in situ* studies of an evolving system. In this respect, the open nature of a synchrotron instrument, with space around the sample to position auxiliary equipment, is an advantage.

2.2.5.1. *Polarization*

Assuming the beam is 100% polarized in the horizontal plane of the synchrotron orbit and with detection in the vertical plane, there is no need for any polarization correction to the diffracted intensities. However, if a small amount of vertical polarization of the beam does need to be taken into account (possibly up to a few per cent depending on the source), the polarization factor that describes its effect on the intensity of the diffracted beam can be derived, following the approach of Azároff (1955) and Yao & Jinno (1982), as

$$P = \frac{1 - dp + dp\cos^2 2\theta\cos^2 2\theta_a}{1 - dp + dp\cos^2 2\theta_a} = \frac{1 - dp + dp\cos^2 2\theta\cos^2 2\theta_a}{1 - dp\sin^2 2\theta_a}, \tag{2.2.3}$$

where dp is the depolarization fraction (*i.e.* the fraction of the total intensity incident on the sample that is vertically polarized), $2\theta_a$ is the Bragg angle of the analyser crystal (if any), and the denominator scales P to unity at 2θ equal to zero (Dwiggins, 1983) and is a constant for any particular experimental setup. If there is no analyser crystal, or we ignore the effect it would have (*i.e.* by putting $2\theta_a = 0$), then

$$P = 1 - dp\sin^2 2\theta.$$

Beamline staff can usually advise on the appropriate values to use. These expressions reduce to the usual polarization factor for unpolarized (dp = 0.5) laboratory X-rays without a monochromator or analyser crystal, $\frac{1}{2}(1 + \cos^2 2\theta)$.

An alternative formulation of equation (2.2.3) considers the ratio of the vertical to horizontal polarization,

$$rp = \frac{dp}{1 - dp} \quad \text{and} \quad dp = \frac{rp}{1 + rp},$$

so that

$$P = \frac{1 + rp\cos^2 2\theta\cos^2 2\theta_a}{1 + rp\cos^2\theta_a}. \tag{2.2.4}$$

Note that rp = 1.0 for unpolarized (laboratory) X-rays. In reality, because the synchrotron beam is near 100% plane polarized, dp and rp have similar values. The same expressions can be used if diffracting and analysing in the horizontal plane, except that now the value of dp or rp is replaced with the value of $(1 - dp)$ or $1/rp$, respectively.

For Debye–Scherrer rings detected on a 2D detector, the azimuthal angle around the ring needs to be taken into account, yielding

$$P = (1 - dp)(\cos^2 2\theta \sin^2 \kappa + \cos^2 \kappa) + dp(\cos^2 2\theta \cos^2 \kappa + \sin^2 \kappa)$$

or

$$P = \frac{(\cos^2 2\theta \sin^2 \kappa + \cos^2 \kappa) + rp(\cos^2 2\theta \cos^2 \kappa + \sin^2 \kappa)}{1 + rp},$$

where κ is the azimuthal angle (zero in the vertical direction) (Rowles *et al.*, 2012).

2.2.5.2. *Radiation damage*

The intensity of the incident beam can be so high that radiation damage becomes a real concern, particularly for samples containing organic molecules, such as pharmaceuticals, or organometallic materials. Radiation damage manifests itself by progressive shifts (often anisotropic) in the peak positions, a general reduction in peak intensities and peak broadening as the sample's crystallinity degrades. With high-resolution data, the effects are easily seen and can appear after only a few seconds in the worst cases. In such circumstances it may be better to use a 1D or 2D PSD to collect data of sufficient statistical quality before the damage is too severe. However, if the highest-resolution data are required, *via* scanning an analyser crystal, then the problem can be alleviated by filling a long capillary with sample and translating it between scans to expose fresh sample to the beam, thus acquiring multiple data sets which can be summed together. Such an approach necessarily requires a sufficient amount of disposable sample. If attempting to study the evolution of a particular part of the sample, *e.g.* undergoing heat treatment in the beam, then substituting fresh sample is not necessarily an option, and radiation damage can be a frustrating hindrance.

2.2.5.3. *Beam heating*

With a photon intensity of the order 10^{12} photons $\text{mm}^{-2}\,\text{s}^{-1}$ incident on the sample – a possible value for the unfocused beam on a beamline based on an insertion device at a modern third-generation source – the power in the beam corresponds to a few mW mm^{-2}. If a small fraction is absorbed by the sample this can represent a significant heat load that becomes troublesome when trying to work with samples at cryogenic temperatures, where heat capacities are relatively low.

As an example, consider a sample of microcrystalline silicon, composed of cubic 1 μm^3 grains irradiated by a 31 keV beam (0.4 Å wavelength) with 10^{12} photons $\text{mm}^{-2}\,\text{s}^{-1}$. The power of the beam is 5 mW mm^{-2} ($31 \times 10^3\ e \times 10^{12}$ W mm^{-2}). The mass absorption coefficient of Si at 0.4 Å wavelength $\mu/\rho \simeq 1.32$ $\text{cm}^2\,\text{g}^{-1}$ (Milledge, 1968) leading to a linear absorption coefficient of 3.1 cm^{-1} (density of Si = 2.33 g cm^{-3}). Any problems with absorption by such a sample might usually be discounted; for a 1-mm-diameter capillary the value of μr is 0.1, assuming the powder density is 2/3 of the theoretical density.

A single 1-μm^3 grain of cross section 1 μm^2 is hit by 10^6 photons s^{-1}, of which a small fraction are absorbed,

$$\begin{aligned}\text{photons absorbed} &= 10^6[1 - \exp(-3.1 \times 10^{-4})] \\ &= 310 \text{ photons s}^{-1},\end{aligned}$$

corresponding to an absorbed power of 1.54×10^{-12} W. Not all this energy is retained; significant amounts are lost as fluorescence, Compton scatter *etc*. Consultation of tables of mass attenuation coefficients and mass energy-absorption coefficients (Hubbell, 1982; Seltzer, 1993) indicates that for Si at 31 keV about 80% of the energy is retained, thus a net heating power of 1.2×10^{-12} W. The mass of the Si grain is 2.33×10^{-15} kg. At ambient temperature, where the specific heat capacity of Si is 704.6 $\text{J kg}^{-1}\,\text{K}^{-1}$, this leads to an instantaneous tendency to increase the temperature by $\sim$0.7 K s^{-1}. At cryogenic temperatures, *e.g.* 10 K, the specific heat capacity is over three orders of magnitude lower, 0.28 $\text{J kg}^{-1}\,\text{K}^{-1}$ (Desai, 1986), leading to a very strong tendency for the temperature to rise (1840 K s^{-1}). The extent of the potential problem varies depending on the real net absorption of energy of the sample at the wavelength being used. However, it is clear that to prevent local beam-heating effects, the absorbed energy must be removed from the sample as efficiently as possible, *i.e.* by having excellent thermal contact between the grains of the sample and the external medium. At cryogenic temperatures this can be accomplished *via* the He exchange gas in the cryostat. Thus, if using a capillary sample, the capillary must either be left unsealed, to allow the He to permeate between the grains of sample, or it must be sealed under He, allowing transport of the heat to the walls of the capillary. Sealing under air, nitrogen, argon or other atmosphere leads to a loss of heat-transport capability when the gas solidifies, with consequent unpredictable behaviour for the sample caused by the beam-heating effects. This can involve significant shifts in peak positions and peak broadening depending on the instantaneous local temperature gradients. The problems tend to be worse at softer energies, where X-ray absorption is generally higher. Notwithstanding the potential problems, good-quality low-temperature data can be measured with appropriate care.

2.2.5.4. *Choice of wavelength*

The tunability of synchrotron radiation allows the wavelength best suited to the measurements to be selected. The collimation of the beam from the source combined with a perfect crystal monochromator lead automatically to high energy resolution, with a narrow wavelength distribution about a mean value. Consequently there are no issues to contend with such as α_1, α_2 doublets or other effects due to a composite incident spectrum, contributing to a relatively simple instrumental peak-shape function. High energy resolution is essential for high 2θ resolution, because, as shown in equation (2.2.1), the effect of the energy envelope is to broaden the diffraction peaks as 2θ increases.

In choosing the wavelength for an experiment, factors to consider include:

(*a*) The optimum operational range for the beamline to be used, which will principally depend on the characteristics of the source.

(*b*) Absorption: choosing a sufficiently hard energy generally reduces absorption and allows the use of a capillary specimen in transmission for a wide range of compounds, *e.g.* those containing transition metals or heavier elements, thus minimizing preferred orientation. Selecting the energy a little way below (in energy) the *K* or L_{III} absorption edge of an element in the sample may help minimize sample absorption. For any sample or series of samples, it is good practice in the planning of the experiment to calculate the linear absorption coefficient to assess the optimum capillary diameter, the wavelength to use and those to avoid.

(*c*) The use of hard energies can be advantageous for penetration through sample environments, although these should normally, as much as possible, be designed with appropriate X-ray windows *etc*. However, when absorbing environments are unavoidable, such as containing a sample in a spinning Pt

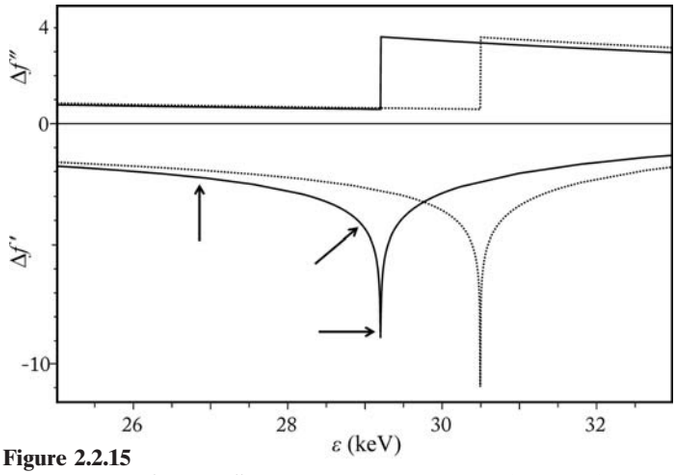

Figure 2.2.15
Variation of $\Delta f'$ and $\Delta f''$ with photon energy for Sn (solid line) and Sb (dotted line) in the vicinity of their K absorption edges (from the tables of Sasaki, 1989). An anomalous-scattering experiment seeking to distinguish the arrangement of the two elements could make measurements at the Sn edge (29.2001 keV), at a few eV below the edge and at an energy significantly removed from the edge (arrows). Equivalent measurements could be made at the Sb edge (30.4912 keV), but as this is above the energy of the Sn edge careful attention must be paid to the increase in the sample's absorption (reflected in the values of $\Delta f''$).

capillary for heating to very high temperatures, then high energy can be a major benefit.

(*d*) Hard energies are essential to measure to high Q values, where $Q = 4\pi \sin\theta/\lambda = 2\pi/d$. For pair distribution function (PDF) analysis, data to $Q > 25$ Å^{-1} ($d < 0.25$ Å) or more are required, with patterns of good statistical quality. Such Q values are not possible with Mo or Ag radiation (Ag $K\alpha$, λ = 0.56 Å, $Q \simeq 22$ Å^{-1} at $2\theta = 160°$), but are easily accessible at λ = 0.4 Å (31 keV) by scanning to $2\theta = 106°$. At 80.7 keV (0.154 Å, ten times shorter than Cu $K\alpha$) patterns to $Q \simeq$ 35 Å^{-1} can be obtained in minutes (even seconds) with a large stationary medical-imaging flat-panel detector (Lee, Aydiner *et al.*, 2008). Even for more classical powder-diffraction experiments, access to data for high Q values can be advantageous for Rietveld refinement of crystal structures, or for measuring several orders of reflections for peak-shape analysis in the investigation of microstructure.

(*e*) Anomalous scattering: performing measurements near the absorption edge of an element in a sample and away from that edge gives element-specific changes in the diffraction intensities, enhancing the experiment's sensitivity to that element (Fig. 2.2.15). The approach can be complimentary to isotopic substitution in a neutron-diffraction experiment or may be the only option when no suitable isotope is available. Good energy resolution is important for these experiments. The values of $\Delta f'$ and $\Delta f''$ vary sharply over only a few eV at the edge, so poor energy resolution would average the abruptly changing values over too broad a range to the detriment of elemental sensitivity and sample absorption if part of the wavelength envelope strays above the edge. Moreover, it is necessary to know accurately where on the edge the measurement is being made to allow the correct values of $\Delta f'$ and $\Delta f''$ to be used in the data analysis. Tables of values have been calculated (*e.g.* Sasaki, 1989), but these do not take account of shifts in an edge due to the oxidation state(s) and chemical environment(s) of the elements. It is advisable to measure the fluorescence of the sample as the energy is scanned through the edge (by varying the monochromator angle θ_m) and then use the Kramers–Kronig relation to calculate the variation of $\Delta f'$ and $\Delta f''$ with energy. A program such as *CHOOCH* (Evans & Pettifer, 2001) allows this to be done.

(*f*) A wavelength greater than 1 Å may be best when working with large unit cells, such as found for proteins, organic molecules or organometallic compounds. Using a long wavelength helps by moving the diffraction pattern to higher 2θ values, away from the zone most affected by background air scatter or masked by the beam stop, and to where the peak asymmetry due to axial beam divergence is less severe. Longer wavelengths are also useful when working in reflection with plate samples to minimize beam penetration and thus enhance sensitivity to the surface regions, *e.g.* in the study of surfaces or coatings.

(*g*) The broad continuous spectrum available from a bending magnet or wiggler allows powder-diffraction measurements *via* the energy-dispersive approach, which is exploited when geometric considerations of the sample or environment mean that a restricted range of 2θ values is accessible or when attempting to obtain the maximum time resolution from a source, as a larger fraction of the photons from the source can be exploited.

2.2.5.5. *Angular resolution*

The highest angular resolution is obtained from a diffractometer equipped with an analyser crystal such as Si(111) or Ge(111). This also gives the robust parallel-beam optical configuration so that peak positions are accurately determined. For well crystallized high-quality samples, peak FWHMs of a few millidegrees are possible, thus maximizing the resolution of reflections with similar d-spacings. For less ideal samples, which represent the majority, microstructural effects broaden the peaks, and indeed high-resolution synchrotron data are exploited for detailed investigation of peak shapes and characterization of a range of properties such as crystallite size, microstrain (Chapter 5.2), defects, chemical homogeneity *etc*. Accurate high-resolution data are particularly useful for solving crystal structures from powders (Chapter 4.1), increasing the possibilities for indexing the powder diffraction pattern (Chapter 3.4), assessing the choice of possible space groups, and providing high-quality data for the structural solution and refinement steps. With a high-resolution pattern, the maximum amount of information is stored in the complex profile composed from the overlapping peaks.

2.2.5.6. *Spatial resolution*

Focusing the X-ray beam gives improved spatial resolution, *e.g.* for studying a small sample contained in a diamond anvil cell at high pressure. A beam with dimensions of a few μm can be obtained, though at the expense of the divergence of the beam arriving at the sample. In such cases the use of a 2D detector to record the entire Debye–Scherrer rings will be required to accumulate the diffraction pattern in a reasonable time and to reveal any problems with preferred orientation or granularity in the sample. With a very small sample only a few grains may be correctly oriented to provide each powder reflection. Alternatively, provided the intensity of the beam is high enough, simply cutting down the beam size with slits may be appropriate, *e.g.* to map residual strain in a weld or mechanical component where a spatial resolution on the 50–100 μm scale may be required. Smaller beam sizes may not be useful if they are comparable to the intrinsic grain size of the material, thus leading

to a poor statistical average of grain orientations and a spotty diffraction pattern.

2.2.5.7. *Time resolution*

The high flux allows powder-diffraction patterns to be measured quickly, opening up the possibilities for time-resolved studies, following the evolution of samples on a timescale, if appropriate, down to milliseconds, *e.g.* to investigate the kinetics and the mechanism of a phase transition caused by a change of the temperature, pressure or other external condition, or a chemical reaction taking place in the sample, such as self-propagating combustion synthesis (Labiche *et al.*, 2007). Many instruments allow great flexibility in the design of experiments to study systems *in situ*, helped by the availability of hard radiation to penetrate through sample environments and reduce the angular range that must be accessed to measure enough diffraction peaks to yield the desired information.

2.2.5.7.1. *Using fast detectors*

Scanning a detector through the d-spacing range of interest necessarily takes a few seconds, so is too slow to measure the fastest processes. Thus, for speed, a multichannel detector system is required that acquires the full diffraction pattern synchronously and that can be read out rapidly, such as *via* a fast PSD or using the energy-dispersive approach. Many different types of detector systems have been exploited for fast powder-diffraction studies using the monochromatic Debye–Scherrer configuration (Section 2.2.4.2), including 1D photodiode arrays (Pennartz *et al.*, 1992; Wong *et al.*, 2006; Palmer *et al.*, 2004), the Mythen curved 1D PSD (Fadenberger *et al.*, 2010), pixel detectors (Yonemura *et al.*, 2006; Terasaki & Komizo, 2011), CCD-based detectors (Malard *et al.*, 2011; Elmer *et al.*, 2007), and medical-imaging detectors (Chupas, Chapman, Jennings *et al.*, 2007; Newton *et al.*, 2010). The former of these last two studies shows that these large detectors working at hard X-ray energies above 60 keV register a wide enough Q range in a single cycle to allow PDF analysis to be made, thus allowing the conduct of time-resolved PDF analysis of, for example, catalytic systems composed of evolving nanoparticles. For the latter study, the diffraction measurements were combined with simultaneous monitoring of the reacting system with the acquisition of complementary mass and diffuse reflectance infrared Fourier transform spectra (DRIFTS).

2.2.5.7.2. *Using the pulse structure*

For investigating very fast, reversible processes, use can be made of the bunch structure of the synchrotron source and the stroboscopic measurement approach. The time for an orbit of an electron circulating in a synchrotron is (circumference/c) s. For a synchrotron such as at the ESRF (with a circumference of 844.4 m), this corresponds to 2.82 µs (*i.e.* a frequency of 355036 Hz). Thus when operating with 16 electron bunches distributed evenly around the ring, there is a burst of X-rays delivered to a beamline every 176 ns, and because of the longitudinal dimension of the electron bunch (∼20 mm), each burst lasts ∼70 ps. Such a pulsed source can be used in pump–probe powder-diffraction experiments, whereby a sample is excited by a short laser pulse (∼100 fs duration) then probed by the X-ray beam a chosen delay time later. The scattered X-rays are recorded with a suitable (probably 2D) detector and the process is repeated, with the statistical quality of the diffraction pattern building up over a number of cycles, after which the detector is read out. A high-speed chopper in the X-ray beam can be used to select the pulse frequency desired for any particular set of measurements. By varying the delay time the evolution of the sample as a function of time after the initial excitation can be investigated. The whole experiment needs fast, accurate electronics to correlate the timing of the firing of the laser, the arrival of the X-ray pulse and the phasing of the chopper.

Examples include the study of 4-(dimethylamino)benzonitrile and 4-(diisopropylamino)benzonitrile (Davaasambuu *et al.*, 2004; Techert & Zachariasse, 2004), whose fluorescence properties indicate that photoexcitation leads to the formation of an intramolecular charge-transfer state. Powder-diffraction patterns were collected over 10-minute periods at a frequency of 897 Hz at delay times ranging from −150 ps (as a reference before the laser excitation) to +2500 ps after excitation. Only about 5% of the molecules are excited by the laser, so the powder-diffraction pattern is from a sample containing both excited and ground-state molecules. Rietveld refinement of the structures from the diffraction patterns gave the fraction of excited molecules as a function of delay time, and the nature of the structural change induced by the photoexcitation. For the isopropyl analogue, an exponential relaxation time of 6.3 (±2.8) ns was observed for the excited molecules (compared to 3.28 ns seen spectroscopically). The main distortion to the molecules was a change in the torsion angle between the diisopropylamino group and the benzene ring, from 13–14° determined from the pre-excitation patterns (14.3° *via* single-crystal analysis) to 10 (±1–2)°.

2.2.5.8. *Beamline evolution*

A beamline at a synchrotron source will certainly evolve in its specifications and capabilities. Users and prospective users should follow updates on a facility's website, or contact the beamline staff, for information concerning possibilities for experiments.

References

Als-Nielsen, J. & McMorrow, D. (2001). *Elements of Modern X-ray Physics*. New York: Wiley.

Authier, A. (2006). *Dynamical theory of X-ray diffraction. International Tables for Crystallography*, Vol. B, *Reciprocal Space*, 1st online ed., ch. 5.1. Chester: International Union of Crystallography.

Azároff, L. V. (1955). *Polarization correction for crystal-monochromatized X-radiation*. *Acta Cryst.* **8**, 701–704.

Balzar, D. & Ledbetter, H. (1993). *Voigt-function modeling in Fourier analysis of size- and strain-broadened X-ray diffraction peaks*. *J. Appl. Cryst.* **26**, 97–103.

Barnes, P., Jupe, A. C., Colston, S. L., Jacques, S. D., Grant, A., Rathbone, T., Miller, M., Clark, S. M. & Cernik, R. J. (1998). *A new three-angle energy-dispersive diffractometer*. *Nucl. Instrum. Methods Phys. Res. B*, **134**, 310–313.

Beaumont, J. H. & Hart, M. (1974). *Multiple Bragg reflection monochromators for synchrotron X radiation*. *J. Phys. E Sci. Instrum.* **7**, 823–829.

Bergamaschi, A., Cervellino, A., Dinapoli, R., Gozzo, F., Henrich, B., Johnson, I., Kraft, P., Mozzanica, A., Schmitt, B. & Shi, X. (2009). *Photon counting microstrip detector for time resolved powder diffraction experiments*. *Nucl. Instrum. Methods Phys. Res. A*, **604**, 136–139.

Bergamaschi, A., Cervellino, A., Dinapoli, R., Gozzo, F., Henrich, B., Johnson, I., Kraft, P., Mozzanica, A., Schmitt, B. & Shi, X. (2010). *The MYTHEN detector for X-ray powder diffraction experiments at the Swiss Light Source*. *J. Synchrotron Rad.* **17**, 653–668.

Bilderback, D. H. (1986). *The potential of cryogenic silicon and germanium X-ray monochromators for use with large synchrotron heat loads*. *Nucl. Instrum. Methods Phys. Res. A*, **246**, 434–436.

Boccaleri, E., Carniato, F., Croce, G., Viterbo, D., van Beek, W., Emerich, H. & Milanesio, M. (2007). *In situ simultaneous Raman/high-resolution X-ray powder diffraction study of transformations occurring in materials at non-ambient conditions*. *J. Appl. Cryst.* **40**, 684–693.

Broennimann, Ch., Eikenberry, E. F., Henrich, B., Horisberger, R., Huelsen, G., Pohl, E., Schmitt, B., Schulze-Briese, C., Suzuki, M., Tomizaki, T., Toyokawa, H. & Wagner, A. (2006). *The PILATUS 1m detector*. *J. Synchrotron Rad.* **13**, 120–130.

Cernik, R. J., Murray, P. K., Pattison, P. & Fitch, A. N. (1990). *A two-circle powder diffractometer for synchrotron radiation with a closed loop encoder feedback system*. *J. Appl. Cryst.* **23**, 292–296.

Cheary, R. W. & Coelho, A. (1992). *A fundamental parameters approach to X-ray line-profile fitting*. *J. Appl. Cryst.* **25**, 109–121.

Chupas, P. J., Chapman, K. W., Jennings, G., Lee, P. L. & Grey, C. P. (2007). *Watching nanoparticles grow: the mechanism and kinetics for the formation of TiO_2-supported platinum nanoparticles*. *J. Am. Chem. Soc.* **129**, 13822–13824.

Chupas, P. J., Chapman, K. W. & Lee, P. L. (2007). *Applications of an amorphous silicon-based area detector for high-resolution, high-sensitivity and fast time-resolved pair distribution function measurements*. *J. Appl. Cryst.* **40**, 463–470.

Collins, S. P., Cernik, R. J., Pattison, P., Bell, A. M. T. & Fitch, A. N. (1992). *A two-circle powder diffractometer for synchrotron radiation on Station 2.3 at the SRS*. *Rev. Sci. Instrum.* **63**, 1013–1014.

Cousins, C. S. G. (1994). *High-resolution diffraction at synchrotron sources: correction for counting losses*. *J. Appl. Cryst.* **27**, 159–163.

Cox, D. E., Hastings, J. B., Cardoso, L. P. & Finger, L. W. (1986). *Synchrotron X-ray powder diffraction at X13A: a dedicated powder diffractometer at the National Synchrotron Light Source*. *Mater. Sci. Forum*, **9**, 1–20.

Cox, D. E., Hastings, J. B., Thomlinson, W. & Prewitt, C. T. (1983). *Application of synchrotron radiation to high resolution powder diffraction and Rietveld refinement*. *Nucl. Instrum. Methods*, **208**, 573–578.

Daniels, J. E. & Drakopoulos, M. (2009). *High-energy X-ray diffraction using the Pixium 4700 flat-panel detector*. *J. Synchrotron Rad.* **16**, 463–468.

Davaasambuu, J., Durand, P. & Techert, S. (2004). *Experimental requirements for light-induced reactions in powders investigated by time-resolved X-ray diffraction*. *J. Synchrotron Rad*. **11**, 483–489.

David, W. I. F. & Matthewman, J. C. (1985). *Profile refinement of powder diffraction patterns using the Voigt function*. *J. Appl. Cryst.* **18**, 461–466.

Desai, P. D. (1986). *Thermodynamic properties of iron and silicon. J. Phys. Chem. Ref. Data*, **15**, 967–983.

Dwiggins, C. W. Jr (1983). *General calculation of the polarization factor for multiple coherent scattering of unpolarized and plane-polarized X-rays*. *Acta Cryst.* A**39**, 773–777.

Elmer, J. W., Palmer, T. A. & Specht, E. D. (2007). *In situ observations of sigma phase dissolution in 2205 duplex stainless steel using synchrotron X-ray diffraction*. *Mat. Sci. Eng. A*, **459**, 151–155.

Evans, G. & Pettifer, R. F. (2001). *CHOOCH: a program for deriving anomalous-scattering factors from X-ray fluorescence spectra*. *J. Appl. Cryst.* **34**, 82–86.

Evans, J. S. O., Francis, R. J., O'Hare, D., Price, S. J., Clark, S. M., Flaherty, J., Gordon, J., Nield, A. & Tang, C. C. (1995). *An apparatus for the study of the kinetics and mechanism of hydrothermal reactions by in situ energy dispersive x-ray diffraction*. *Rev. Sci. Instrum.* **66**, 2442–2445.

Fadenberger, K., Gunduz, I. E., Tsotsos, C., Kokonou, M., Gravani, S., Brandstetter, S., Bergamaschi, A., Schmitt, B., Mayrhofer, P. H., Doumanidis, C. C. & Rebholz, C. (2010). *In situ observation of rapid reactions in nanoscale Ni–Al multilayer foils using synchrotron radiation*. *Appl. Phys. Lett.* **97**, 144101.

Glazov, V. M. & Pashinkin, A. S. (2001). *The thermophysical properties (heat capacity and thermal expansion) of single-crystal silicon*. *High Temp.* **39**, 413–419.

Gozzo, F., De Caro, L., Giannini, C., Guagliardi, A., Schmitt, B. & Prodi, A. (2006). *The instrumental resolution function of synchrotron radiation powder diffractometers in the presence of focusing optics*. *J. Appl. Cryst.* **39**, 347–357.

Gullikson, E. M. (2001). *Atomic scattering factors*. *X-ray Data Booklet*, edited by A. C. Thompson & D. Vaughan. Lawrence Berkeley National Laboratory, USA. http://xdb.lbl.gov/Section1/Sec_1-7.pdf.

Hastings, J. B., Thomlinson, W. & Cox, D. E. (1984). *Synchrotron X-ray powder diffraction*. *J. Appl. Cryst.* **17**, 85–95.

Häusermann, D. & Barnes, P. (1992). *Energy-dispersive diffraction with synchrotron radiation: optimization of the technique for dynamic studies of transformations*. *Phase Transit.* **39**, 99–115.

Hewat, A. W. (1975). *Design for a conventional high-resolution neutron powder diffractometer*. *Nucl. Instrum. Methods*, **127**, 361–370.

Hewat, A. W. (1979). *Absorption corrections for neutron diffraction*. *Acta Cryst.* A**35**, 248.

Hodeau, J.-L., Bordet, P., Anne, M., Prat, A., Fitch, A. N., Dooryhée, E., Vaughan, G. & Freund, A. (1998). *Nine-crystal multianalyzer stage for high-resolution powder diffraction between 6 keV and 40 keV*. *Proc. SPIE*, **3448**, 353–361.

Honkimäki, V. & Suortti, P. (2007). *Energy-dispersive diffraction with synchrotron radiation and a germanium detector*. *J. Synchrotron Rad.* **14**, 331–338.

Hubbell, J. H. (1982). *Photon mass attenuation and energy-absorption coefficients*. *Int. J. Appl. Radiat. Isot.* **33**, 1269–1290.

Ida, T., Hibino, H. & Toraya, H. (2001). *Peak profile function for synchrotron X-ray diffractometry*. *J. Appl. Cryst.* **34**, 144–151.

Ida, T., Hibino, H. & Toraya, H. (2003). *Deconvolution of instrumental aberrations for synchrotron powder X-ray diffractometry*. *J. Appl. Cryst.* **36**, 181–187.

Kim, K.-J. (2001). *Characteristics of synchrotron radiation*. *X-ray Data Booklet*, edited by A. C. Thompson & D. Vaughan. Lawrence Berkeley National Laboratory, USA. http://xdb.lbl.gov/Section2/Sec_2-1.html.

Kirkpatrick, P. & Baez, A. V. (1948). *Formation of optical images by X-rays*. *J. Opt. Soc. Am.* **38**, 766–774.

Koopmans, K. & Rieck, G. D. (1968). *International Tables for X-ray Crystallography*, Vol. III, edited by C. H. MacGillavry & G. D. Rieck, pp. 194–195. Birmingham: Kynoch Press.

Korsunsky, A. M., Song, X., Hofmann, F., Abbey, B., Xie, M., Connolley, T., Reinhard, C. R. C., Atwood, R. C., Connor, L. & Drakopoulos, M. (2010). *Polycrystal deformation analysis by high energy synchrotron X-ray diffraction on the I12 JEEP beamline at Diamond Light Source*. *Mater. Lett.* **64**, 1724–1727.

Labiche, J.-C., Mathon, O., Pascarelli, S., Newton, M. A., Ferre, G. G., Curfs, C., Vaughan, G., Homs, A. & Carreiras, D. F. (2007). *The fast readout low noise camera as a versatile X-ray detector for time resolved dispersive extended X-ray absorption fine structure and diffraction studies of dynamic problems in materials science, chemistry, and catalysis*. *Rev. Sci. Instrum.* **78**, 091301–1–11.

Langford, J. I. (1978). *A rapid method for analysing the breadths of diffraction and spectral lines using the Voigt function*. *J. Appl. Cryst.* **11**, 10–14.

Laundy, D. & Collins, S. (2003). *Counting statistics of X-ray detectors at high counting rates*. *J. Synchrotron Rad.* **10**, 214–218.

Lee, J. H., Aydiner, C. C., Almer, J., Bernier, J., Chapman, K. W., Chupas, P. J., Haeffner, D., Kump, K., Lee, P. L., Lienert, U., Miceli, A. & Vera, G. (2008). *Synchrotron applications of an amorphous silicon flat-panel detector*. *J. Synchrotron Rad.* **15**, 477–488.

Lee, P. L., Shu, D., Ramanathan, M., Preissner, C., Wang, J., Beno, M. A., Von Dreele, R. B., Ribaud, L., Kurtz, C., Antao, S. M., Jiao, X. & Toby, B. H. (2008). *A twelve-analyzer detector system for high-resolution powder diffraction*. *J. Synchrotron Rad.* **15**, 427–432.

Lengeler, B., Schroer, C., Tümmler, J., Benner, B., Richwin, M., Snigirev, A., Snigireva, I. & Drakopoulos, M. (1999). *Imaging by parabolic refractive lenses in the hard X-ray range*. *J. Synchrotron Rad.* **6**, 1153–1167.

Lipson, H. (1967). *International Tables for X-ray Crystallography*, Vol. II, edited by J. S. Kasper & K. Lonsdale, pp. 291–292. Birmingham: Kynoch Press.

Malard, B., Pilch, J., Sittner, P., Delville, R. & Curfs, C. (2011). *In situ investigation of the fast microstructure evolution during electropulse treatment of cold drawn NiTi wires*. *Acta Mater.* **59**, 1542–1556.

Margaritondo, G. (1988). *Introduction to Synchrotron Radiation.* Oxford University Press.

Masson, O., Dooryhée, E. & Fitch, A. N. (2003). *Instrument line-profile synthesis in high-resolution synchrotron powder diffraction*. *J. Appl. Cryst.* **36**, 286–294.

Milledge, H. J. (1968). *International Tables for X-ray Crystallography*, Volume III, *Physical and Chemical Tables*, edited by C. H. MacGillavry, G. D. Rieck & K. Lonsdale, pp. 175–192. Birmingham: Kynoch Press.

Mills, D. M., Helliwell, J. R., Kvick, Å., Ohta, T., Robinson, I. A. & Authier, A. (2005). *Report of the Working Group on Synchrotron Radiation Nomenclature - brightness, spectral brightness or brilliance?* *J. Synchrotron Rad.* **12**, 385.

Newton, M. A., Di Michiel, M., Kubacka, A. & Fernández-García, M. (2010). *Combining time-resolved hard X-ray diffraction and diffuse*

reflectance infrared spectroscopy to illuminate CO dissociation and transient carbon storage by supported Pd nanoparticles during CO/NO cycling. *J. Am. Chem. Soc.* **132**, 4540–4541.

Newton, M. A. & van Beek, W. (2010). *Combining synchrotron-based X-ray techniques with vibrational spectroscopies for the in situ study of heterogeneous catalysts: a view from a bridge*. *Chem. Soc. Rev.* **39**, 4845–4863.

Palmer, T. A., Elmer, J. W. & Babu, S. S. (2004). *Observation of ferrite/austenite transformations in the heat affected zone of 2205 duplex stainless steel spot welds using time resolved X-ray diffraction*. *Mater. Sci. Eng. A*, **374**, 307–321.

Parrish, W. (1988). *Advances in synchrotron X-ray polycrystalline diffraction*. *Aust. J. Phys.* **41**, 101–112.

Parrish, W. & Hart, M. (1987). *Advantages of synchrotron radiation for polycrystalline diffractometry*. *Z. Kristallogr.* **179**, 161–173.

Parrish, W., Hart, M., Erickson, C. G., Masciocchi, N. & Huang, T. C. (1986). *Instrumentation for synchrotron X-ray powder diffractometry*. *Adv. X-ray Anal.* **29**, 243–250.

Pennartz, P. U., Löchner, U., Fuess, H. & Wroblewski, T. (1992). *Powder diffraction in the range of milliseconds*. *J. Appl. Cryst.* **25**, 571–577.

Rijssenbeek, J., Gao, Y., Zhong, Z., Croft, M., Jisrawi, N., Ignatov, A. & Tsakalakos, T. (2011). *In situ X-ray diffraction of prototype sodium metal halide cells: time and space electrochemical profiling*. *J. Power Sources*, **196**, 2332–2339.

Rowles, M. R., Styles, M. J., Madsen, I. C., Scarlett, N. V. Y., McGregor, K., Riley, D. P., Snook, G. A., Urban, A. J., Connolley, T. & Reinhard, C. (2012). *Quantification of passivation layer growth in inert anodes for molten salt electrochemistry by in situ energy-dispersive diffraction*. *J. Appl. Cryst.* **45**, 28–37.

Sabine, T. M. (1987*a*). *The N-crystal spectrometer*. *J. Appl. Cryst.* **20**, 23–27.

Sabine, T. M. (1987*b*). *A powder diffractometer for a synchrotron source*. *J. Appl. Cryst.* **20**, 173–178.

Sabine, T. M., Hunter, B. A., Sabine, W. R. & Ball, C. J. (1998). *Analytical expressions for the transmission factor and peak shift in absorbing cylindrical specimens*. *J. Appl. Cryst.* **31**, 47–51.

Sasaki, S. (1989). *Numerical Tables of Anomalous Scattering Factors Calculated by the Cromer and Liberman Method*. KEK Report, 88–14, 1–136.

Scarlett, N. V. Y., Madsen, I. C., Evans, J. S. O., Coelho, A. A., McGregor, K., Rowles, M., Lanyon, M. R. & Urban, A. J. (2009). *Energy-dispersive diffraction studies of inert anodes*. *J. Appl. Cryst.* **42**, 502–512.

Seltzer, S. M. (1993). *Calculation of photon mass energy-transfer and mass energy-absorption coefficients*. *Radiat. Res.* **136**, 147–170.

Snigirev, A. A., Filseth, B., Elleaume, P., Klocke, Th., Kohn, V., Lengeler, B., Snigireva, I., Souvorov, A. & Tuemmler, J. (1997). *Refractive lenses for high-energy X-ray focusing*. *Proc. SPIE*, **3151**, 164–170.

Snigirev, A., Kohn, V., Snigireva, I., Souvorov, A. & Lengeler, B. (1998). *Focusing high-energy X rays by compound refractive lenses*. *Appl. Opt.* **37**, 653–662.

Spiller, E. (2000). *X-ray optics*. *Adv. X-ray Anal.* **42**, 297–307.

Techert, S. & Zachariasse, K. A. (2004). *Structure determination of the intramolecular charge transfer state in crystalline 4-(diisopropylamino) benzonitrile from picosecond X-ray diffraction*. *J. Am. Chem. Soc.* **126**, 5593–5600.

Terasaki, H. & Komizo, Y. (2011). *Diffusional and displacive transformation behaviour in low carbon-low alloy steels studied by a hybrid in situ observation system*. *Scr. Mater.* **64**, 29–32.

Thompson, P., Cox, D. E. & Hastings, J. B. (1987). *Rietveld refinement of Debye–Scherrer synchrotron X-ray data from Al_2O_3*. *J. Appl. Cryst.* **20**, 79–83.

Vaughan, G. B. M., Wright, J. P., Bytchkov, A., Rossat, M., Gleyzolle, H., Snigireva, I. & Snigirev, A. (2011). *X-ray transfocators: focusing devices based on compound refractive lenses*. *J. Synchrotron Rad.* **18**, 125–133.

Walton, R. I. & O'Hare, D. (2000). *Watching solids crystallise using in situ powder diffraction*. *Chem. Commun.* pp. 2283–2291.

Wong, J., Larson, E. M., Waide, P. A. & Frahm, R. (2006). *Combustion front dynamics in the combustion synthesis of refractory metal carbides and di-borides using time-resolved X-ray diffraction*. *J. Synchrotron Rad.* **13**, 326–335.

Wright, J., Vaughan, G. & Fitch, A. (2003). *Merging data from a multi-detector continuous scanning powder diffraction system*. *International Union of Crystallography Commission on Crystallographic Computing Newsletter*, **1**, 92–96.

Wroblewski, T. (1991). *Resolution functions of powder diffractometers at a synchrotron-radiation source*. *Acta Cryst.* A**47**, 571–577.

Yamanaka, T. & Ogata, K. (1991). *Structure refinement of GeO_2 polymorphs at high pressures and temperatures by energy-dispersive spectra of powder diffraction*. *J. Appl. Cryst.* **24**, 111–118.

Yao, T. & Jinno, H. (1982). *Polarization factor for the X-ray powder diffraction method with a single-crystal monochromator*. *Acta Cryst.* A**38**, 287–288.

Yonemura, M., Osuki, T., Terasaki, H., Komizo, Y., Sato, M. & Toyokawa, H. (2006). *Two-dimensional time-resolved X-ray diffraction study of directional solidification in steels*. *Mater. Trans.* **47**, 2292–2298.

Zachariasen, W. H. (1945). *Theory of X-ray Diffraction in Crystals*. Dover Publications Inc.